Research Square

Preprints are preliminary reports that have not undergone peer review.
They should not be considered conclusive, used to inform clinical practice,
or referenced by the media as validated information.

Genipin-Crosslinked Gelatin-Mediated Immobilization of Vancomycin/Rifampin Microspheres on 3D-Printed Porous Tantalum Scaffolds for Local Antibacterial Prophylaxis in Bone Repair

Zhenchao Xu
Hunan Children's Hospital
Guanghui Zhu
Hunan Children's Hospital
Dingyu Jiang
Xiangya Hospital Central South University
Yilu Zhang
Xiangya Hospital Central South University
Zheng Liu
Hunan Children's Hospital
Xiyang Wang
wqlwqwxy@163.com

Xiangya Hospital Central South University

Article

Keywords: 3D printing, Porous tantalum, Antibiotic microspheres, Local drug delivery, Biofilm inhibition, Osteogenesis

Posted Date: November 13th, 2026

DOI: https://doi.org/10.21203/rs.3.rs-11567222/v1

License: This work is licensed under a Creative Commons Attribution 4.0 International License.
Read Full License

Additional Declarations: No competing interests reported.

Genipin-Crosslinked Gelatin-Mediated Immobilization of Vancomycin/Rifampin Microspheres on 3D-Printed Porous Tantalum Scaffolds for Local Antibacterial Prophylaxis in Bone Repair

Zhenchao Xu[1, 2], Guanghui Zhu[1, 2], Dingyu Jiang[3], Yilu Zhang[3], Zheng Liu[1, 2*], Xiyang Wang[3*]

1. Department of Pediatric Orthopedics, The Affiliated Children's Hospital of Xiangya School of Medicine, Central South University (Hunan Children's Hospital), Changsha, Hunan, 410007, China.

2. Hunan Provincial Key Laboratory of Pediatric Orthopedics, Hunan Children's Hospital, Changsha, Hunan, 410007, China.

3. Department of Spine Surgery and Orthopaedics, Xiangya Hospital of Central South University, Changsha, Hunan 410008, China;

Corresponding author:

Zheng Liu[*]

Correspondence: liuzheng_0629@sina.com

Xiyang Wang[*]

Correspondence: wqlwqwxy@163.com

Abstract

Implant-associated infections and insufficient osseointegration remain critical challenges in orthopedic surgery. This study developed a multifunctional scaffold by immobilizing vancomycin- and rifampin-loaded PLGA/PLLA core–shell microspheres onto 3D-printed porous tantalum (Ta) via a genipin-crosslinked gelatin coating. The composite scaffold (pTa-Gle@MS) exhibited a hierarchical porous architecture and achieved sustained, sequential dual-antibiotic release over 27 days *in vitro*, with an initial burst release followed by a gradual release phase. *In vitro* antibacterial assays against *Staphylococcus aureus* demonstrated that pTa-Gle@MS markedly reduced planktonic and adherent bacteria and inhibited biofilm formation, achieving a 95.1 ± 3.2% reduction in bacterial counts, whereas bare and gelatin-coated Ta showed no antimicrobial activity. Cytocompatibility and osteogenic differentiation assays in MC3T3-E1 cells revealed that the functionalized scaffold supported cell adhesion, proliferation, and osteogenesis comparably to unmodified porous Ta, with no significant differences in collagen secretion, ALP activity, mineralization, or osteogenic gene expression ($P > 0.05$). In a non-infected rat femoral condyle defect model, pTa-Gle@MS maintained local therapeutic antibiotic concentrations at 6 weeks without detectable systemic accumulation in the liver or kidney and achieved new bone ingrowth and osseointegration at 12 weeks comparable to control scaffolds, as confirmed by micro-CT and histological analysis. These findings indicate that gelatin-mediated integration of antibiotic microspheres confers *in vitro* antibacterial and antibiofilm activity on 3D-printed porous Ta without compromising its inherent osteoconductivity. Further evaluation in infected or contaminated defect models is required to determine its in vivo infection-prevention efficacy.

Keywords: 3D printing; Porous tantalum; Antibiotic microspheres; Local drug delivery, Biofilm inhibition; Osteogenesis

Implant-associated bone infection remains a formidable challenge in orthopedic surgery and imposes substantial clinical and economic burdens worldwide. With the increasing use of orthopedic implants, the risk of deep surgical site infection has become a critical

contributor to treatment failure, prolonged hospitalization, and even mortality[1, 2]. The infection rate after internal fixation of open fractures can reach 27%, whereas periprosthetic joint infection occurs in 0.2%–2.2% of total hip arthroplasties, and surgical site infection affects 2%–5% of spinal procedures [3, 4]. Conventional systemic antibiotic therapy is often inadequate because poor vascularization at the infection site results in subtherapeutic local drug concentrations, poor patient compliance, and the emergence of drug-resistant bacteria[5]. These limitations highlight the urgent need for localized and sustained antibacterial strategies that can simultaneously support bone regeneration.

Local drug delivery systems based on biodegradable carriers offer a promising approach to overcoming these challenges [6]. Among these systems, core–shell microspheres enable controlled sequential antibiotic release, maintaining effective local concentrations over extended periods while minimizing systemic toxicity[7]. Poly (lactic-co-glycolic acid) (PLGA) and poly (L-lactic acid) (PLLA) have been widely investigated as carrier materials because of their excellent biocompatibility, tunable degradation profiles, and established fabrication protocols[8]. Compared with traditional antibiotic-loaded bone cement, PLGA-based delivery systems have demonstrated a superior ability to sustain drug release above the minimum inhibitory concentration without interfering with bone healing. Vancomycin and rifampin were selected for encapsulation because of their synergistic activity against Staphylococcus aureus, which accounts for 50%–55% of orthopedic implant-related infections[9]. Core–shell microspheres were prepared via coaxial electrospraying to achieve sequential antibiotic release, thereby enhancing antibacterial efficacy and reducing the development of resistance.

In parallel, an ideal bone graft substitute must provide adequate mechanical support, promote osseointegration, and possess inherent or conferred antimicrobial properties [10]. Porous metallic implants, particularly those fabricated via additive manufacturing (3D printing), offer significant advantages for bone repair. Their interconnected porous architectures can be tailored to match the elastic modulus of native bone and reduce stress shielding, whereas their high surface area facilitates osteoblast adhesion,

proliferation, and bone ingrowth[11-13]. Tantalum (Ta) has emerged as a leading material in this category due to its outstanding biocompatibility, corrosion resistance, and favorable mechanical properties. Porous Ta scaffolds have demonstrated excellent clinical performance in promoting osseointegration in joint arthroplasty and revision surgeries[14, 15]. However, the same porosity that supports bone regeneration also provides an ideal substrate for bacterial adhesion and biofilm formation [16]. Ta lacks intrinsic antibacterial activity, making established infections exceedingly difficult to eradicate with systemic antibiotics alone and often leading to implant failure and revision surgery [14, 16, 17].

Surface functionalization with bioactive coatings provides a viable strategy for integrating antimicrobial capability into porous Ta scaffolds without compromising their osteoconductive properties[18]. Gelatin, a natural polymer derived from collagen, is an attractive coating material because of its biocompatibility, biodegradability, hydrophilicity, and ease of processing[19]. It can serve as an effective interfacial layer for immobilizing drug-loaded microspheres onto the scaffold surface, thereby creating a composite system that combines structural support with localized therapeutic delivery [20, 21].

Several antibacterial modification strategies for porous Ta have been reported, including direct vancomycin loading, anti-tuberculosis drug coating, and metal ion doping [22, 23]. These studies support the feasibility of antibacterial functionalization of porous Ta, but most available approaches rely on a single drug, non-programmed release, or ion-mediated antibacterial mechanisms, and therefore may provide limited temporal control or raise concerns regarding dose-dependent cytotoxicity. In contrast, a strategy that immobilizes vancomycin/rifampin core–shell microspheres to on porous Ta to achieve staged dual-antibiotic release while preserving the osteoconductive structure of the scaffold has less fully explored. To address this gap, the present study proposes a composite design in which vancomycin- and rifampin-loaded PLGA/PLLA core–shell microspheres are immobilized onto 3D-printed porous tantalum scaffolds through a gelatin coating. This construct is intended to combine the osteoconductive framework of porous Ta with sustained local antibacterial delivery for infection

prophylaxis in high-risk bone defect reconstruction, rather than to claim therapeutic efficacy against established infection at this stage. The gelatin coating is intended to ensure uniform attachment of microspheres and may further enhance the interfacial microenvironment. This positioning also explains the use of a non-infected *in vivo* defect model in the present work, which was designed to first assess safety and osseointegration before subsequent validation in infected models.

The present work systematically evaluates the physicochemical properties, drug release kinetics, antibacterial efficacy (with a focus on biofilm inhibition), cytocompatibility, osteogenic potential, and *in vivo* osseointegration performance of this functionalized scaffold. The findings are expected to provide a preclinical basis for developing porous Ta implants that combine preserved bone-regenerative capacity with local antibacterial prophylactic potential, while recognizing that direct evidence in infected bone defects remains to be established.

Materials and methods

2.1 ***Fabrication of porous tantalum scaffolds via selective laser melting***

Two types of cylindrical porous tantalum scaffolds based on a triangular prism unit cell were designed and fabricated. The first type measured 10 mm in diameter and 5 mm in height, whereas the second type measured 5 mm in diameter and 2.5 mm in height. Both scaffold types had a designed pore size of 500 μm and an internal porosity of approximately 60%.

The scaffolds were manufactured using a selective laser melting (SLM) system (Hunan Farsoon High-Technology Co., Ltd., China). Pure tantalum powder (Research Institute of Powder Metallurgy, Central South University, China), with a particle size distribution of 15–53 μm and confirmed to be dry and oxide-free, was used as the raw material. Three-dimensional models were designed using SolidWorks CAD software (Dassault Systèmes, France) and exported in STL format. The model data were imported into the SLM equipment, where the proprietary slicing software segmented the models into 20-μm-thick layers. Fabrication was performed under an argon atmosphere. The processing parameters, including laser power, scan speed, and hatch spacing, were optimized to

obtain fully dense struts. The powder was melted layer by layer and subsequently solidified.

Post-processing involved the following steps. First, support structures were carefully removed using specialized tools. The as-built scaffolds were then ultrasonically cleaned sequentially with acetone, anhydrous ethanol, and deionized water for 15 min each to remove residual powder and impurities. After drying, the scaffolds were subjected to stress-relief annealing in a sintering furnace (FCT Systems, Germany). The temperature was increased to 600 °C at 5 °C/min, held for 1 h, and then furnace-cooled.

2.2 ***Preparation of vancomycin/rifampin-loaded core-shell microparticles***

Core–shell microparticles loaded with vancomycin and rifampin were fabricated using a coaxial electrostatic spraying technique. For the shell solution, the liposoluble drug rifampin (Sigma-Aldrich, United States) was directly dissolved in a dichloromethane solution containing PLGA (Mw: 40 kDa; Sigma-Aldrich, United States), typically by adding 100 mg of rifampin to 10 mL of the PLGA/DCM solution to obtain a 1% (w/v) rifampin loading solution.

The core emulsion was prepared by dissolving the water-soluble drug, vancomycin (Sigma-Aldrich, United States), in double-distilled water at 50 mg/mL. This aqueous phase was then emulsified with a 10% (w/v) PLLA (Sigma-Aldrich, United States) solution in ethyl acetate at an aqueous-to-organic volume ratio of 1:9 under ice-bath conditions using a probe ultrasonicator to form a uniform water-in-oil (W/O) emulsion. For electrostatic spraying and particle collection, the PLLA emulsion (core phase) and PLGA solution (shell phase) were separately loaded into syringes and delivered to the inner and outer channels of a coaxial stainless-steel needle (inner tube inner/outer diameter: 0.20/0.40 mm; outer tube inner/outer diameter: 0.50/0.72 mm) at flow rates of 1.5 mL/h using syringe pumps. A 10 kV high-voltage source was applied to the needle tip to generate a stable Taylor cone. Microparticle formation and morphology were monitored in real time using an optical microscope. The resulting microparticles were collected in an anhydrous ethanol bath, centrifuged, washed three times with double-distilled water, redispersed, snap-frozen, lyophilized for 72 h, sterilized with ethylene oxide, and stored at 4 °C until further use. The microspheres prepared by this

coaxial electrospray protocol have been systematically characterized in our previous study, including particle size distribution, encapsulation efficiency, actual drug loading, and core–shell morphology [24].

2.3 ***Fabrication of 3D-printed porous tantalum scaffolds loaded with dual-antibiotic microparticles***

The composite scaffolds were prepared by integrating antibiotic microparticles into porous tantalum scaffolds using a gelatin (Shanghai Acmec Biochemical Technology Co., Ltd., China) carrier. First, 20 mg of lyophilized vancomycin/rifampin core–shell microparticles was weighed. A 5% (w/v) gelatin solution was prepared by dissolving gelatin in double-distilled water at 37 °C. The porous tantalum scaffold was placed in a custom-sized polytetrafluoroethylene mold. The microparticles were thoroughly mixed with the warm gelatin solution, and the mixture was carefully injected into the scaffold under gentle agitation to ensure complete infiltration and uniform distribution. The construct was then frozen and lyophilized for 3 days. After lyophilization, the scaffold was immersed in a 1% (w/v) genipin solution (Shanghai Acmec Biochemical Technology Co., Ltd., China) and crosslinked in the dark at room temperature for 12 h. Finally, the crosslinked composite scaffold was rinsed three times with anhydrous ethanol, air-dried, and stored in a desiccator. The preparation process is illustrated in Figure 1.

2.4 ***Experimental groups***

Three groups were established in this study: 3D-printed porous tantalum scaffolds loaded with dual-antibiotic microspheres (pTa-Gle@MS), gelatin-coated 3D-printed porous tantalum scaffolds (pTa-Gle), and uncoated porous tantalum scaffolds (pTa), which served as the control group.

2.5 ***Morphological characterization of scaffolds***

The prepared scaffolds were sputter-coated with gold, mounted on specimen stubs, and observed using scanning electron microscopy (SEM) (Czech FEI) to examine their microstructure. Energy-dispersive X-ray spectroscopy (EDS) (Bruke Germany) was used to analyze the elemental composition of each scaffold group.

2.6 ***In vitro drug release assay***

The composite scaffolds (pTa-Gle@MS) were placed in dialysis bags and immersed in centrifuge tubes containing 10 mL of phosphate-buffered saline (PBS). The tubes were incubated at 37 °C with shaking at 120 rpm on an orbital shaker. At predetermined time points (1, 2, 4, 6, 8, 11, 14, 18, 22, and 27 days), 5 mL of release medium was collected and immediately replaced with an equal volume of fresh PBS. The collected samples were stored at −20 °C until analysis. The concentrations of released vancomycin and rifampicin were determined using a spectrophotometer at wavelengths of 280 nm and 474 nm, respectively. The cumulative release percentage was calculated as the ratio of released drug to the total theoretical drug loading, and release profiles were plotted accordingly.

2.7 ***Material preparation and cell culture***

MC3T3-E1 osteogenic precursor cells (Cell Resource Center, Shanghai Institutes of Biological Sciences, Chinese Academy of Sciences, China) were cultured in α-MEM supplemented with 10% fetal bovine serum (Gibco, United States) and 1% penicillin-streptomycin (streptomycin and penicillin at 100 U/mL; Hyclone, United States). Cells were maintained at 37 °C in a humidified atmosphere containing 5% CO_2. The medium was refreshed every 2 days. Cells were harvested using trypsin and counted with an automated cell counter to prepare cell suspensions at the required densities for subsequent experiments.

2.8 ***Cell adhesion observed by confocal laser scanning microscopy (CLSM)***

Sterilized scaffolds (n=3 per group) were placed in 24-well plates, prewetted with complete medium for 24 h, and then seeded with MC3T3-E1 cells at a density of 1×10^6 cells per scaffold in 100 μL of suspension (1×10^6 cells/mL). After an additional 900 μL of medium was added, the cells were co-cultured for 24 h. The samples were then washed with PBS, fixed with 4% paraformaldehyde for 10 min, and permeabilized with 0.1% Triton X-100 in PBS. F-actin was stained with Actin-Tracker Green (diluted 1:100 in PBS containing 5% BSA and 0.1% Triton X-100) for 30 min in the dark. Nuclei were counterstained with 1 μg/mL DAPI for 5 min. After washing, the samples were imaged using CLSM (Zeiss, Germany) to visualize cytoskeletal morphology and cell adhesion on the scaffold surfaces.

2.9 ***Cell viability assay (live/dead staining)***

Cell-seeded scaffolds prepared as described in Section 2.8 were cultured for 1 and 3 days. At each time point, the culture medium was replaced with a freshly prepared staining solution containing 2μM Calcein-AM and 3μM propidium iodide (PI) (Beyotime Biotechnology, China) in 1× Assay Buffer. After incubation at room temperature for 30 min in the dark, the samples were washed and immediately observed under a fluorescence microscope to distinguish live cells (green) from dead cells (red).

2.10 ***Cell proliferation assay (CCK-8)***

Cell proliferation on the scaffolds was evaluated using a Cell Counting Kit-8 (CCK-8). Scaffolds seeded with cells as described above were cultured for 1, 3, 5, and 7 days. At each time point, the medium was replaced with a 1:10 dilution of CCK-8 reagent (Dojindo, Japan) in fresh medium. After 4 h of incubation, 100 μL of supernatant from each well was transferred to a 96-well plate, and absorbance at 450 nm was measured using a microplate reader.

2.11 ***Evaluation of osteogenic differentiation***

For all osteogenic differentiation assays, cells were seeded onto scaffolds at a density of 5×10^6 cells per scaffold. After 24 h of attachment, the complete medium was replaced with osteogenic induction medium containing α-MEM, 10nM dexamethasone, 50 μg/mL ascorbic acid, and 10 mM β-glycerophosphate. The induction medium was refreshed every 3 days.

*2.*12 ***Collagen deposition assay by Sirius red staining***

After 7 days of induction, the samples were fixed with 4% paraformaldehyde and stained with Sirius Red solution (Beyotime Biotechnology, China) for 1 h. After washing, stained collagen was dissolved in elution buffer (0.2 M NaOH: methanol = 1:1), and the absorbance at 540 nm was measured.

2.13 ***Alkaline phosphatase (ALP) activity***

After 7 and 14 days of induction, the cells were lysed with 0.1% Triton X-100 in PBS. The lysates were centrifuged, and the supernatants were collected. ALP activity was quantified using a commercial ALP assay kit (Beyotime Biotechnology, China) according to the manufacturer's instructions by measuring absorbance at 405 nm.

2.14 ***Calcium nodule formation assay by Alizarin red S staining***

After 21 and 28 days of induction, the samples were fixed and stained with 2% Alizarin Red Staining solution (Cyagen Biosciences, United States) for 30 min. After thorough washing, the calcium-bound dye was dissolved in 10% cetylpyridinium chloride, and absorbance at 620 nm was measured.

2.15 ***Quantitative real-time PCR (qPCR)***

After 14 days of induction, total RNA was extracted from cells on the scaffolds using TRIzol reagent. RNA purity and concentration were determined spectrophotometrically. cDNA was synthesized using a reverse transcription kit with gDNA eraser. qPCR was performed using SYBR Premix Ex Taq II on a real-time PCR system. The gene expression levels of Runx2, Osteocalcin (OCN), and Osteopontin (OPN) were analyzed, with β-actin serving as the internal control. Primer sequences are listed in Table 1. Relative gene expression was calculated using the 2^(-ΔΔCt) method.

2.16 ***Bacterial culture preparation***

Staphylococcus aureus (BeNa Culture Collection, BNCC 186335) was used for the antibacterial assays. Frozen stock was rapidly thawed at 37 °C, inoculated into LB broth, and incubated overnight at 37 °C with shaking at 220 rpm. Bacterial purity was confirmed by streaking the culture onto Tryptic Soy Agar (TSA) plates and incubating at 37 °C for 24 h. For subsequent experiments, bacterial suspensions were adjusted to the desired concentrations in sterile PBS using a densitometer.

2.17 ***Antibacterial activity of composite scaffolds***

Sterilized scaffolds (n=3 per group) were placed in 24-well plates and incubated with 1 mL of S. aureus suspension (1×10^6 CFU/mL) at 37 °C for 24 h.

Plate Count Method: After incubation, the scaffolds were rinsed with PBS to remove non-adherent bacteria, transferred to centrifuge tubes containing PBS, and subjected to ultrasonication for 10 min to detach adherent bacteria. The resulting eluates were diluted in series, plated on TSA, and incubated for 24 h. Colony-forming units (CFU) were then counted, and the bacterial inhibition rate was calculated.

Live/Dead Bacterial Staining: After 24 h of co-culture, bacterial viability on the scaffolds was assessed using a SYTO 9/PI staining kit (Beyotime Biotechnology, China)

according to the manufacturer's instructions. Stained samples were observed under a fluorescence microscope.

Inhibition Zone Test: Bacterial lawns were prepared on TSA plates using 100 μL of S. aureus suspension (1×10^7 CFU/mL). The scaffolds were placed at the center of each plate and incubated at 37 °C for 24 h. The diameter of the clear inhibition zone surrounding each scaffold was measured.

2.18 ***Inhibition of bacterial biofilm formation***

Scaffolds (n=3 per group) were incubated with 1 mL of S. aureus suspension (1×10^7 CFU/mL) in LB broth at 37 °C for 24 h to allow biofilm formation. After gentle washing with PBS, the biofilms were fixed with 4% paraformaldehyde for 20 min, dried for 12 h, and stained with 0.5% crystal violet for 10 min. Excess stain was removed by washing with PBS. For qualitative analysis, the stained biofilms were visualized under a microscope. For quantitative analysis, bound crystal violet was dissolved in 33% acetic acid, and absorbance was measured at 575 nm.

2.19 ***Animal model and surgical procedure***

Twenty-four 8-week-old male Sprague-Dawley rats weighing 300–400 g were obtained from the Department of Laboratory Animals of Central South University and randomly divided into three groups (n=8 per group): pTa-Gle@MS, pTa-Gle, and pTa. Under anesthesia induced by intraperitoneal injection of pentobarbital sodium (3% w/v solution; 45 mg/kg), a critical-sized bone defect measuring 5 mm in diameter and 2.5 mm in depth was created in the lateral femoral condyle using a high-speed drill under saline irrigation. Sterilized scaffolds were implanted into the defects, and the incisions were sutured (Figure 2). Penicillin (80,000 U/day) was administered intramuscularly for 3 days postoperatively to in all groups to prevent nonspecific postoperative infection. Therefore, the animal experiment was designed to evaluate local drug retention, safety, and osseointegration in a non-infected defect model, rather than to directly test in *vivo* antibacterial efficacy.

2.20 ***Specimen collection***

Calcein and alizarin red were injected subcutaneously 1 week before euthanasia. At 6 and 12 weeks after implantation, animals were euthanized by gradual inhalation of 100%

CO_2 in a dedicated transparent euthanasia chamber (Shanghai Yuyan Scientific Instrument Co., Ltd., China; model CL-1000M) connected to a calibrated flow meter. CO_2 was delivered at a displacement rate of 20% of the chamber volume per minute until respiratory arrest, and exposure was continued for at least 2 min after respiratory arrest. Death was confirmed by cervical dislocation before specimen collection. No other chemical euthanasia agents were administered. Euthanasia was performed in accordance with the institutional animal care guidelines and the AVMA Guidelines for the Euthanasia of Animals. The femoral condyles containing the implants were harvested for analysis. For the pTa-Gle@MS group, surrounding muscle, liver, and kidney tissues were also collected for subsequent analysis of drug concentrations *via* High-Performance Liquid Chromatography (HPLC). Samples were weighed, homogenized in an appropriate volume of PBS, and deproteinized with acetonitrile. After centrifugation and filtration, the supernatant was injected into the HPLC system (Waters Pacific Pte Ltd., Singapore). Separation was performed on a reversed-phase C18 column at 30 °C using an isocratic mobile phase of PBS and acetonitrile (70:30, v/v) at a flow rate of 1.0 mL/min. Analytes were detected at 240 nm (Van) and 334 nm (Rif) using a UV-Vis or photodiode array detector. Quantification was performed using external standard calibration curves.

2.21 ***Radiographic and micro-CT analysis***

Harvested specimens were fixed in 4% paraformaldehyde and subjected to X-ray radiography and high-resolution micro-CT scanning at an isotropic voxel size of 18 μm. Three-dimensional reconstruction and quantitative analysis were performed using CTAn software to determine bone tissue parameters, including trabecular thickness (Tb.Th), trabecular number (Tb.N), and bone volume fraction (BV/TV).

2.22 ***Histological processing***

The fixed bone samples were dehydrated through a graded ethanol series (70%, 95%, and 100%), embedded in polymethylmethacrylate (PMMA), and sectioned into 200-μm slices. The slices were then ground and polished to a final thickness of 50 μm for histological and CLSM observation.

2.23 ***Histological staining***

Van Gieson (VG) and Hematoxylin & Eosin (H&E) Staining: Sections were stained using standard VG and H&E protocols to visualize new bone formation and general tissue morphology. Stained sections were observed under a light microscope. The area of new bone formation within the scaffold region was quantified using ImageJ software (NIH, United States) and expressed as a percentage of the total region of interest.

2.24 ***Statistical analysis***

All quantitative data are expressed as the mean ± standard deviation ($x \pm s$). Statistical analysis was performed using SPSS software (version 22.0). Normality and homogeneity of variance were assessed where applicable before parametric comparisons. For comparisons among three groups at a single time point, one-way analysis of variance was used, followed by an appropriate post hoc multiple-comparison test when the overall difference was significant. For outcomes involving both group and time factors, the time effect and group-by-time relationship were interpreted with consideration of the experimental design, and intergroup comparisons were reported at each prespecified time point. A *P* value of less than 0.05 was considered statistically significant.

Results

3.1 ***Characterization of 3D-printed porous tantalum scaffolds loaded with dual-antibiotic microspheres***

The macroscopic appearance of the scaffolds in each group is shown in Figure 3. The genipin-crosslinked 3D-printed porous tantalum scaffold loaded with dual-antibiotic microspheres (pTa-Gle@MS) exhibited the darkest color, which was attributable to the blue-black hue produced by the reaction between gelatin and genipin. The gelatin-coated porous tantalum scaffold (pTa-Gle) appeared lighter than pTa-Gle@MS but darker than the bare porous tantalum scaffold (pTa).

3.2 ***Surface morphology and elemental composition***

SEM images revealed the surface morphology of the scaffolds (Figure 4a). The pTa-Gle@MS surface displayed a lamellar porous structure with numerous adherent microspheres. A similar lamellar porous structure was observed on pTa-Gle. In contrast,

the pTa surface appeared relatively smooth, with visible tantalum powder particles. Energy-dispersive X-ray spectroscopy (EDS) analysis (Figure 4b) indicated the presence of Ta, O, C, Cl, and N in pTa-Gle@MS; H was not detected. The detection of Cl and N was consistent with the composition of rifampin and vancomycin. The pTa-Gle scaffold contained Ta, O, and C, whereas only Ta and O were detected in pTa.

3.3 ***In vitro drug release profile***

The drug release profiles of the pTa-Gle@MS scaffold at various time points are shown in Figure 5. The release trend was similar to that of the Van/Rif microsphere group. This sequential release behavior is consistent with the core–shell architecture and release kinetics quantitatively characterized for the same microsphere system in our previous study [24]. An initial burst release was observed, although the release curve was slightly more gradual than that of microspheres alone. Subsequently, the release rates of both antibiotics decreased and approached the release profile of the free microspheres, indicating that gelatin-mediated immobilization did not abolish the sustained-release behavior of the microspheres.

3.4 ***Cell adhesion observed by CLSM***

Cell morphology was assessed using FITC-phalloidin/DAPI staining. Under low magnification, cells on all scaffolds exhibited clear cytoplasm, plump nuclei, and mature morphology with a networked actin filament structure. High-magnification images showed no significant differences in the green fluorescent actin cytoskeleton among the groups (Figure 6), indicating that the scaffolds had no adverse effects on cell adhesion.

3.5 ***Live/dead cell staining***

Calcein AM/PI staining revealed robust osteoblast adhesion to all scaffolds (Figure 7a). After 3 days of co-culture, cell density increased markedly in all groups, with no apparent dead cells observed. These results suggest increased cell viability from day 1 to day 3 and the absence of cytotoxicity for all scaffolds.

3.6 ***CCK-8 assay***

The CCK-8 assay (Figure 7b) showed a continuous increase in cell number after 1, 3, 5, and 7 days of co-culture with the scaffolds. No significant differences in OD values

were detected among the groups at any time point (P>0.05), suggesting that microsphere immobilization and gelatin/genipin coating did not produce detectable cytotoxicity under the present *in vitro* conditions.

3.7 ***Collagen secretion***

Sirius Red staining after 7 days of osteogenic induction (Figure 8a) and quantitative analysis (Figure 8b) showed no significant differences in collagen secretion among the groups (P>0.05), suggesting that the composite scaffold did not affect early osteogenic differentiation.

3.8 ***ALP activity***

Quantitative ALP assays performed after 7 and 14 days of osteogenic induction (Figure 8c) revealed no significant intergroup differences (P>0.05), indicating that the composite scaffold did not measurably impair early- to mid-stage osteogenic differentiation.

3.9 ***Mineralization nodule formation***

Quantification of mineralized nodules after 21 and 28 days of osteogenic induction (Figure 8d) showed no significant differences among groups (P>0.05), suggesting that the scaffold did not influence late-stage osteogenic differentiation, including matrix mineralization.

3.10 ***Osteogenic gene expression***

qPCR analysis of osteogenic genes (Runx2, OCN, and OPN) showed no significant differences in expression levels among the groups (P>0.05; Figure 8e), indicating that the composite scaffold did not alter osteogenic differentiation at the transcriptional level.

3.11 ***Antibacterial efficacy: plate counting***

After 24 h of co-culture with S. aureus, bacterial adhesion was quantified by plate counting (Figure 9a). No significant difference was observed between pTa-Gle and pTa (P>0.05). However, pTa-Gle@MS showed significantly fewer bacterial colonies than both pTa-Gle and pTa (P<0.01; Figure 9b and 9c), with an inhibition rate of 95.1 ± 3.2%.

3.12 ***Live/dead bacterial staining***

Fluorescent staining (Figure 9d) showed weak green fluorescence, representing live

bacteria, and strong red fluorescence, representing dead bacteria, in the pTa-Gle@MS group. In contrast, pTa-Gle and pTa exhibited strong green fluorescence with negligible red fluorescence, further confirming the potent antibacterial activity of pTa-Gle@MS.

3.13 ***Inhibition zone test***

The pTa-Gle@MS scaffold formed an inhibition zone with a diameter of 2.53 ± 0.17 cm, whereas no inhibition zones were observed for pTa-Gle or pTa (Figure 9e).

3.14 ***Biofilm formation***

After 1 day of co-culture in LB medium, continuous dark purple biofilms were observed on pTa-Gle and pTa, with no significant quantitative difference between the two groups (Figure 9f). In contrast, pTa-Gle@MS showed minimal biofilm formation, with a significantly lower quantitative value than the other groups ($P<0.01$, Figure 9g).

3.15 ***In vivo drug concentration***

The concentrations of vancomycin and rifampin in the femoral condyle and surrounding muscle tissues at various time points after pTa-Gle@MS implantation are summarized in Table 2. Antibiotics were detected locally at 6 weeks but were undetectable at 12 weeks. No antibiotics were detected in liver or kidney samples, suggesting limited systemic accumulation under the present experimental conditions.

3.16 ***Radiographic evaluation***

X-ray images obtained at 6 and 12 weeks postoperatively (Figure 10) showed stable implant positioning without loosening, displacement, periprosthetic fracture, or distal femoral osteolysis.

Micro-CT and 3D reconstruction results (Figure 11a and 11b) showed minimal new bone formation around all scaffolds at 6 weeks, with translucent gaps still visible and limited bone ingrowth into the pores. By 12 weeks, the scaffolds were surrounded by substantial new bone, with evident bone ingrowth into the pores, indicating progressive bone–scaffold integration. Three-dimensional reconstruction confirmed an increase in bone volume over time. Morphologically, no significant differences were observed among the groups at the same time point. Tb.Th, Tb.N, and BV/TV increased significantly over time in all groups ($P<0.05$), with no intergroup differences at each time point ($P>0.05$, Figure 11c). These results indicate preserved, rather than superior,

osseointegration after antibacterial functionalization.

3.17 ***Fluorescent labeling of bone formation***

Calcein labeling (Figure 12) showed weak fluorescence within the scaffold pores at 6 weeks, with sporadic stronger signals at the scaffold–bone interface. Fluorescence intensity increased markedly within the pores by 12 weeks, indicating progressive new bone ingrowth. No significant differences in fluorescence intensity were observed among the groups at the same time point, further supporting that the coating and antibiotic microspheres did not impair bone formation in the non-infected model.

3.18 ***Histological analysis***

H&E and VG staining (Figure 13a and 13b) revealed the presence of osteoblasts within the scaffold pores at 6 weeks, but mature bone tissue was not observed. By 12 weeks, mature bone tissue had grown into the pores and closely integrated with the scaffold, with no evidence of bone necrosis.

Quantification of the percentage of new bone area at 6 and 12 weeks (Figure 13c) showed no statistically significant differences among the three groups ($P>0.05$).

Discussion

The development of ideal bone graft substitutes remains a major challenge in orthopedics and reconstructive surgery. An optimal material must satisfy a triad of critical requirements: excellent biocompatibility to avoid immune rejection and support cellular functions, mechanical properties comparable to those of native bone to ensure structural integrity, and a three-dimensional porous architecture that promotes osteoconduction, vascularization, and eventual osseointegration[25]. Although metallic implants, particularly those based on titanium and its alloys, cobalt-chromium, and stainless steel, have long been the cornerstone of load-bearing orthopedic implants, limitations related to elastic modulus mismatch, stress shielding, and insufficient biological integration have driven the search for advanced alternatives[26]. In this context, Ta has emerged as a promising candidate because of its exceptional corrosion resistance, inherent biocompatibility, and favorable interactions with bone cells[27]. The spontaneous formation of a stable, hydrophilic Ta_2O_5 layer upon exposure to

oxygen not only confers remarkable inertness but also enhances osteoblast adhesion, proliferation, and differentiation[28-30]. However, bulk tantalum has an excessively high elastic modulus (approximately 188 GPa), far exceeding that of cortical bone (7–30 GPa), which can lead to stress shielding and subsequent bone resorption [15].

To address this issue, the advent of additive manufacturing, particularly SLM, has revolutionized the fabrication of porous metallic scaffolds. SLM enables the precise digital fabrication of complex, patient-specific geometries with controlled pore architecture, thereby overcoming the limitations of traditional manufacturing methods, including lack of personalization, structural inhomogeneity, and poor interconnectivity[31]. For bone regeneration, scaffold architectural parameters, primarily pore size, porosity, and interconnectivity, are critical. These features govern mechanical strength, nutrient diffusion, cell migration, and tissue ingrowth. Evidence from extensive *in vitro* and *in vivo* studies suggests an optimal pore size range of 300–600 μm for bone formation, with approximately 500 μm often providing the best compromise between mechanical integrity and biological performance [32, 33]. Similarly, although high porosity (>80%) is beneficial for cell infiltration and vascularization, it can substantially compromise mechanical strength. Therefore, a porosity range of 60-80% is frequently targeted to balance these competing requirements [34, 35]. Consistent with these findings, the present study used SLM to fabricate porous Ta scaffolds with a prismatic unit cell design, an average pore size of 500 μm, and a porosity of 60%. This design yielded an elastic modulus of approximately 9.2 GPa, closely matching that of human cortical bone, and a compressive strength suitable for load-bearing applications, thereby mitigating the risk of stress shielding.

Despite these excellent osteogenic properties, a major limitation of porous Ta, as with other orthopedic implants, is susceptibility to bacterial colonization and infection. The high surface area and porous structure, although ideal for tissue integration, can also provide niches for bacterial adhesion and biofilm formation, which are leading causes of implant failure[36]. To confer antibacterial functionality without compromising biocompatibility, a local, sustained antibiotic delivery system is highly

desirable. Several approaches have been explored to enhance the antibacterial capability of porous tantalum scaffolds[15, 37]. Current strategies for improving the antimicrobial properties of porous Ta primarily focus on surface coating techniques, alloying, and incorporation of bioactive substances. Among these, surface coating technology is one of the most widely applied methods for antibacterial modification of porous Ta scaffolds. For instance, Hua et al. [21]developed a composite scaffold by loading the anti-tuberculosis drugs isoniazid and rifampicin onto gellan gum, which was then coated onto 3D-printed porous Ta modified with a polydopamine layer to enhance adhesion. This design enabled localized, long-term, and controllable drug release while supporting bone regeneration. Similarly, Liu et al. [25]used chemical grafting to functionalize porous Ta with vancomycin, resulting in a composite scaffold capable of rapidly eradicating initially adhered bacteria and resisting biofilm formation, thereby facilitating prompt infection control and modulating the immune microenvironment. This scaffold also exhibited good biocompatibility and favorable osteogenic induction *in vitro*.

The introduction of bioactive substances represents another effective approach for enhancing the antibacterial performance of porous Ta. Studies have shown that incorporating agents such as drugs or ions can significantly improve antimicrobial outcomes. For example, Fialho et al. [16] applied a zinc oxide coating onto porous Ta by magnetron sputtering, which effectively inhibited bacterial growth while maintaining good biocompatibility in cytotoxicity assays. Alternatively, the incorporation of specific metal ions has been investigated. Cui et al. [14] fabricated Ta-Cu alloy scaffolds that exhibited notable antibacterial properties attributable to copper ions, which can trigger beneficial ion-mediated antibacterial responses through compositional tuning. Silver, known for its potent antibacterial activity, has also been used. Di et al. [38] coated porous Ta scaffolds with a thin silver nanoparticle film and confirmed enhanced antibacterial efficacy.

Notably, any modification intended to improve the antibacterial properties of porous Ta must carefully balance antimicrobial performance with biocompatibility. Sustained release of metal ions may pose potential cytotoxicity risks, whereas the

introduction of bioactive substances could lead to unintended side effects [39]. Therefore, a comprehensive evaluation of both antibacterial efficiency and biocompatibility is essential to ensure the safe and broad application of modified porous Ta materials in clinical settings. Core-shell microspheres fabricated by coaxial electrospraying offer an elegant solution. This technique allows encapsulation of different drugs in distinct compartments, namely the core and shell, within a single microsphere, enabling sophisticated control over release kinetics[40, 41]. By encapsulating a hydrophilic antibiotic, vancomycin, in the core and a lipophilic antibiotic, rifampicin, in the shell—or vice versa—using biodegradable polymers such as PLLA and PLGA, we engineered dual-drug delivery vehicles. The processing parameters, including voltage, flow rate, and solution properties such as viscosity and surface tension, were meticulously optimized to produce microspheres with uniform size and morphology and high encapsulation efficiency[42-44]. In our previous work, this coaxial electrospray system was systematically characterized with respect to particle size, encapsulation efficiency, drug loading, core–shell structure, and sequential release kinetics; together with the antibacterial results reported therein, these data provide materials-level support for the core–shell architecture, staged release, and sustained antibacterial potential of the microsphere component observed at the scaffold level in the present study [24].

The final step in creating a multifunctional implant involved integrating the antibiotic-loaded microspheres with the 3D-printed porous Ta scaffold. Surface modification of Ta is challenging due to its chemical inertness. Gelatin, a denatured collagen derivative, was selected as the coating material due to its excellent biocompatibility, biodegradability, and bioadhesive properties[45, 46]. To improve mechanical stability and delay degradation, gelatin was crosslinked with genipin, a natural, biocompatible crosslinking agent known to be less cytotoxic than alternatives such as glutaraldehyde [47]. The genipin-crosslinked gelatin formed a porous hydrogel layer on the Ta struts, serving as an ideal matrix for incorporation and retention of the antibiotic microspheres [48]. This composite design yielded a scaffold with a hierarchical structure: the macroporous Ta backbone provides mechanical support, the

meso-/microporous gelatin hydrogel enhances biocompatibility and cellular interaction, and the embedded microspheres act as localized antibiotic depots.

Evaluation of this composite scaffold confirmed its intended multifunctional design. Importantly, incorporation of the gelatin coating and antibiotic microspheres did not impair the excellent biocompatibility or osteogenic potential of the underlying porous Ta. *In vitro*, the composite scaffold supported osteoblast adhesion, proliferation, and differentiation to an extent comparable to that of uncoated porous Ta and gelatin-coated Ta scaffolds, as verified by CCK-8 assays, cytoskeletal observation, and osteogenic marker expression. These findings indicate that the modifications did not introduce cytotoxic components or hinder the favorable cell-material interactions inherent to porous Ta. Simultaneously, the composite scaffold exhibited robust antibacterial activity *in vitro*, effectively reducing planktonic and adherent *S. aureus* and preventing biofilm formation. These results should be interpreted as evidence of in vitro antibacterial and antibiofilm potential, rather than direct proof of in vivo infection resistance. In the non-infected rat femoral condyle defect model, local vancomycin and rifampin remained detectable at 6 weeks without detectable liver or kidney accumulation, suggesting local retention with limited systemic exposure. However, the *in vivo* drug-concentration findings are not directly equivalent to the 27-day in vitro release profile, because drug diffusion, tissue binding, scaffold retention, and degradation differ between PBS release conditions and living tissue. Histological analysis using H&E and VG staining revealed comparable new bone formation and osseointegration among the composite scaffold, gelatin-coated Ta, and bare porous Ta groups. Although some studies suggest that gelatin can actively promote bone healing [49], the similar bone formation observed across groups in the present study suggests that the porous Ta architecture remained the primary osteoconductive driver. The role of the gelatin coating may be more facilitative, improving the initial interfacial environment without negatively affecting osteogenesis. The absence of significant inhibition of bone growth by the antibiotic-releasing composite is a critical finding, demonstrating successful dissociation of antimicrobial function from osteogenic function.

Several limitations of this study should be acknowledged. First, the antibacterial evaluation was restricted to a single reference strain of *S. aureus*; the efficacy against methicillin-resistant *S. aureus* (MRSA), coagulase-negative staphylococci, clinical isolates, or polymicrobial biofilms remains to be investigated. Second, the *in vivo* bone defect model was non-infected, and all groups received postoperative penicillin for 3 days; therefore, the animal experiment cannot be used to demonstrate *in vivo* infection-prevention or treatment efficacy in a contaminated surgical environment. Future studies employing infected or contaminated-defect models are required to validate the clinical potential of this scaffold as an infection-resistant implant. Third, the mechanical properties of the composite scaffold, particularly fatigue resistance under cyclic loading after gelatin coating and microsphere incorporation, were not systematically evaluated, which is critical for load-bearing applications. Fourth, *in vitro* release was quantified using UV-visible spectrophotometry rather than a more specific chromatographic method, and future work should use HPLC or LC-MS-based assays to better correlate in vitro release with in vivo tissue concentrations. Finally, this study was conducted in a small-animal model; large-animal studies with functional loading are necessary to establish the translational relevance of this approach.

In summary, this study developed and characterized a multifunctional porous Ta-based scaffold by combining SLM-fabricated porous Ta, coaxially electrosprayed vancomycin/rifampin-loaded microspheres, and a genipin-crosslinked gelatin adhesive interface. The resulting composite scaffold achieved sustained local antibiotic release *in vitro*, showed antibacterial and antibiofilm activity against *S. aureus in vitro*, and preserved the cytocompatibility, osteogenic differentiation, and osseointegration capacity of porous Ta in a non-infected rat bone defect model. The present evidence supports the scaffold as a promising platform for local antibacterial prophylaxis in bone repair, but it does not yet establish therapeutic efficacy in infected defects. Further work should focus on optimizing drug-loading ratios and release kinetics, validating efficacy in infected or contaminated animal defect models, assessing long-term mechanical and fatigue stability after coating degradation, and conducting large-animal load-bearing studies to determine translational feasibility.

Data availability statement

The data that support the findings of this study are available from the corresponding authors upon reasonable request.

Ethics statement

The animal study was carried out in strict accordance with the guidelines and ethical approval of the Animal Ethics Committee of Hunan Children's Hospital (No. HCHDWLL-2024-04). Animal housing and maintenance protocols followed the local authority guidelines.

Author contributions

Z.C.X.: Conceptualization, Experiment, Data curation, Formal analysis, Writing - original draft. G.H.Z.: Supervising, and Writing - review. D.Y.J. and Y.L.Z.: Data curation, Formal analysis. Z.L. and X.Y.W.: Funding acquisition, Investigation, Writing - editing. All authors discussed the results and commented on the manuscript.

Funding

This work was supported by the National Key Research and Development Program of China (2023YFC2507605), the Hunan Provincial Key Laboratory of Pediatric Orthopedics (2023TP1019), the Health Research Project of Hunan Provincial Health Commission (W20243175).

Competing interests

The authors declare no competing interests.

References

1. Norris, G. R. et al. Prevalence of deep surgical site infection after repair of periarticular knee fractures: a systematic review and meta-analysis. JAMA Netw. Open 2, e199951 (2019).

2. Li, B. & Webster, T. J. Bacteria antibiotic resistance: new challenges and opportunities for implant-associated orthopedic infections. J. Orthop. Res. 36, 22–32 (2018).

3. Davidson, D. J. Understanding Periprosthetic Joint Infection. (UCL, 2024).

4. Willey, M. & Karam, M. Impact of infection on fracture fixation. Orthop. Clin. 47, 357–364 (2016).

5. Gatti, M. et al. Orthopaedic implant-associated staphylococcal infections: a critical reappraisal of unmet clinical needs associated with the implementation of the best antibiotic choice. Antibiotics 11, 406 (2022).

6. Chen, C. et al. Nano-thin amorphous tantalum-coated prosthesis for acetabular bone defect reconstruction: in vivo study and case series. Front. Bioeng. Biotechnol. 13, 1687455 (2025).

7. Chen, P. et al. Development, optimization, and pharmacokinetics study of bufalin/nintedanib co-loaded modified albumin sub-microparticles fabricated by coaxial electrostatic spray technology. AAPS PharmSciTech 23, 13 (2021).

8. Elmowafy, E. M., Tiboni, M. & Soliman, M. E. Biocompatibility, biodegradation and biomedical applications of poly(lactic acid)/poly(lactic-co-glycolic acid) micro and nanoparticles. J. Pharm. Investig. 49, 347–380 (2019).

9. Cardoso, G. C. et al. Current strategies in developing antibacterial surfaces for joint arthroplasty implant applications. (2024).

10. Zhao, R. et al. Bone grafts and substitutes in dentistry: a review of current trends and developments. Molecules 26, 3007 (2021).

11. Bandyopadhyay, A. et al. Porous metal implants: processing, properties, and challenges. Int. J. Extrem. Manuf. 5, 032014 (2023).

12. Zerankeshi, M. M., Bakhshi, R. & Alizadeh, R. Polymer/metal composite 3D porous bone tissue engineering scaffolds fabricated by additive manufacturing techniques: a review. Bioprinting 25, e00191 (2022).

13. Feng, Y. et al. Application of 3D printing technology in bone tissue engineering: a review. Curr. Drug Deliv. 18, 847–861 (2021).

14. Cui, J. et al. Antibacterial activity, corrosion resistance and wear behavior of spark

plasma sintered Ta-5Cu alloy for biomedical applications. J. Mech. Behav. Biomed. Mater. 74, 315–323 (2017).

15. Huang, G., Pan, S.-T. & Qiu, J.-X. The clinical application of porous tantalum and its new development for bone tissue engineering. Materials 14, 2647 (2021).

16. Fialho, L. et al. Porous tantalum oxide with osteoconductive elements and antibacterial core-shell nanoparticles: a new generation of materials for dental implants. Mater. Sci. Eng. C 120, 111761 (2021).

17. Gao, Y. et al. Bioinspired porous microspheres for sustained hypoxic exosomes release and vascularized bone regeneration. Bioact. Mater. 14, 377–388 (2022).

18. Han, Q. et al. Porous tantalum and titanium in orthopedics: a review. ACS Biomater. Sci. Eng. 5, 5798–5824 (2019).

19. Castro-Maria, A., Fernandez-Blazquez, J. P. & Patterson, J. Genipin-crosslinked gelatin hydrogels with controlled molecular weight: a strategy to balance processability and performance. Gels 11, (2025).

20. Holmkvist, A. D. et al. Hydrophobic ion pairing of a minocycline/Ca^{2+}/AOT complex for preparation of drug-loaded PLGA nanoparticles with improved sustained release. Int. J. Pharm. 499, 351–357 (2016).

21. Hua, L. et al. 3D-printed porous tantalum coated with antitubercular drugs achieving antibacterial properties and good biocompatibility. Macromol. Biosci. 22, e2100338 (2022).

22. Li, X. et al. Progress of research on the surface functionalization of tantalum and porous tantalum in bone tissue engineering. Biomed. Mater. 19, (2024).

23. Liang, D. et al. Fabrication of porous tantalum with low elastic modulus and tunable pore size for bone repair. ACS Biomater. Sci. Eng. 9, 1720–1728 (2023).

24. Xu, Z., Wang, X., Zhu, G. & Liu, Z. Osteogenic and antibacterial effects of double antibiotic-loaded microspheres. Sci. Rep. 16, 27042 (2026).

25. Liu, B. et al. Experimental study of a 3D printed permanent implantable porous Ta-coated bone plate for fracture fixation. Bioact. Mater. 10, 269–280 (2022).

26. Bazaka, O. et al. Metallic implants for biomedical applications. (2021).

27. Liu, T. et al. Biofunctionalization of 3D printed porous tantalum using a

vancomycin-carboxymethyl chitosan composite coating to improve osteogenesis and antibiofilm properties. ACS Appl. Mater. Interfaces 14, 41764–41778 (2022).

28. Li, X. et al. Progress of research on the surface functionalization of tantalum and porous tantalum in bone tissue engineering. Biomed. Mater. 19, 042009 (2024).

29. Kummer, N. et al. Engineering nanoscale frontiers: valve metal oxide nanostructures from fundamentals to multifunctional biomedical applications. Chem. Rec. e70185 (2026).

30. Rahmati, B. Development of Tantalum Oxide (Ta-o) Thin Film Coating on Biomedical Ti-6Al-4V Alloy to Enhance Mechanical and Tribological Properties, and Biocompatibility. (University of Malaya, 2016).

31. Zhou, J. et al. Customized additive manufacturing in bone scaffolds—the gateway to precise bone defect treatment. Research 6, 0239 (2023).

32. Sebastiani, S. et al. Structural influences on bone tissue engineering: a review and perspective. Matter 8, (2025).

33. Yu, H.-P. & Zhu, Y.-J. Guidelines derived from biomineralized tissues for design and construction of high-performance biomimetic materials: from weak to strong. Chem. Soc. Rev. 53, 4490–4606 (2024).

34. Qian, H. et al. Fabrication, bacteriostasis and osteointegration properties researches of the additively-manufactured porous tantalum scaffolds loading vancomycin. Bioact. Mater. 24, 450–462 (2023).

35. Qin, Y. et al. A metamaterial scaffold beyond modulus limits: enhanced osteogenesis and angiogenesis of critical bone defects. Nat. Commun. 16, 2180 (2025).

36. Ran, Q. et al. Osteogenesis of 3D printed porous Ti6Al4V implants with different pore sizes. J. Mech. Behav. Biomed. Mater. 84, 1–11 (2018).

37. Sautet, P. et al. Antibiotic-loaded tantalum may serve as an antimicrobial delivery agent. Bone Joint J. 101-B, 848–851 (2019).

38. Di, H. et al. Ag nanoparticles incorporated tannic acid/nanoapatite composite coating on Ti implant surfaces for enhancement of antibacterial and antioxidant properties. Surf. Coat. Technol. 399, 126169 (2020).

39. Tabrizian, P., Davis, S. & Su, B. From bone to nacre—development of biomimetic

materials for bone implants: a review. Biomater. Sci. 12, 5680–5703 (2024).
40. Tantai, M. et al. Enhancing osteogenesis using 3D-printed porous tantalum scaffolds: a biomechanical, in vivo, and in vitro study. Int. J. Bioprinting 11, 499–514 (2025).
41. Abdullah, M. F. et al. Core-shell fibers: design, roles, and controllable release strategies in tissue engineering and drug delivery. Polymers 11, (2019).
42. van der Kooij, R. S. et al. An overview of the production methods for core-shell microspheres for parenteral controlled drug delivery. Eur. J. Pharm. Biopharm. 170, 24–42 (2022).
43. Wang, X. et al. Advances in surface modification of tantalum and porous tantalum for rapid osseointegration: a thematic review. Front. Bioeng. Biotechnol. 10, 983695 (2022).
44. Wang, X., Ning, B. & Pei, X. Tantalum and its derivatives in orthopedic and dental implants: osteogenesis and antibacterial properties. Colloids Surf. B 208, 112055 (2021).
45. Liu, Y. et al. Modification and crosslinking of gelatin-based biomaterials as tissue adhesives. Colloids Surf. B 174, 316–323 (2019).
46. Lou, L. & Chen, H. Functional modification of gelatin-based biodegradable composite films: a review. Food Addit. Contam. Part A 40, 928–949 (2023).
47. Yu, Y. et al. Genipin-cross-linked hydrogels based on biomaterials for drug delivery: a review. Biomater. Sci. 9, 1583–1597 (2021).
48. Swetha, S. et al. An insight into cell-laden 3D-printed constructs for bone tissue engineering. J. Mater. Chem. B 8, 9836–9862 (2020).
49. Wu, E. et al. Application of gelatin-based composites in bone tissue engineering. Heliyon 10, (2024).

Table 1. Primer sequences used for the detection of osteogenesis-related gene expression.

Genes	Primer sequence
Runx2	F: 5'- ACTCCAAGACCCTAAGAAACCGAT-3'
	R: 5'- TGGCTCCTCCCTTCTCAACCTC-3'
OCN	F: 5'- GAACAGACAAGTCCCACACAGC-3'
	R: 5'- TCAGCAGAGTGAGCAGAAAGAT-3'
OPN	F: 5'- CTCAGAATTCAGCCAGGAGAAC-3'
	R: 5'- CCAAACAGGCAAAAGCAAAT-3'
Actin	F: 5'- ACATCCGTAAAGACCTCTATGCC-3'
	R: 5'- TACTCCTGCTTGCTGATCCAC-3'

Table 2. Drug concentrations in tissues of the pTa-Gle@MS group at different time points (μg/mL)

Tissue	Drug	6W	12W
Femur	vancomycin	15.3±1.7	Not detected
	rifampicin	20.4±1.9	Not detected
Muscle	vancomycin	14.1±1.6	Not detected
	rifampicin	18.6±2.1	Not detected

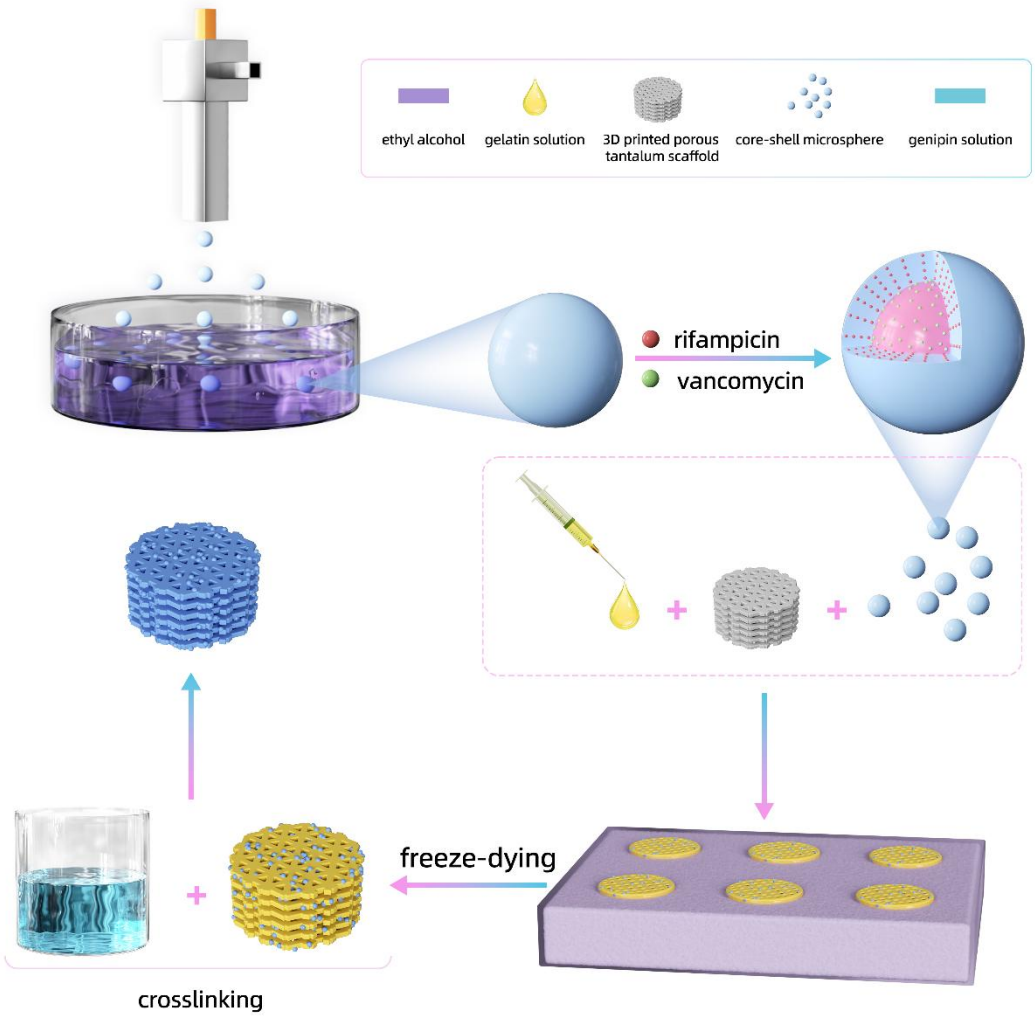


Figure 1. Fabrication of a 3D-Printed Porous Tantalum Composite Scaffold Loaded with Dual-Antibiotic Microspheres.

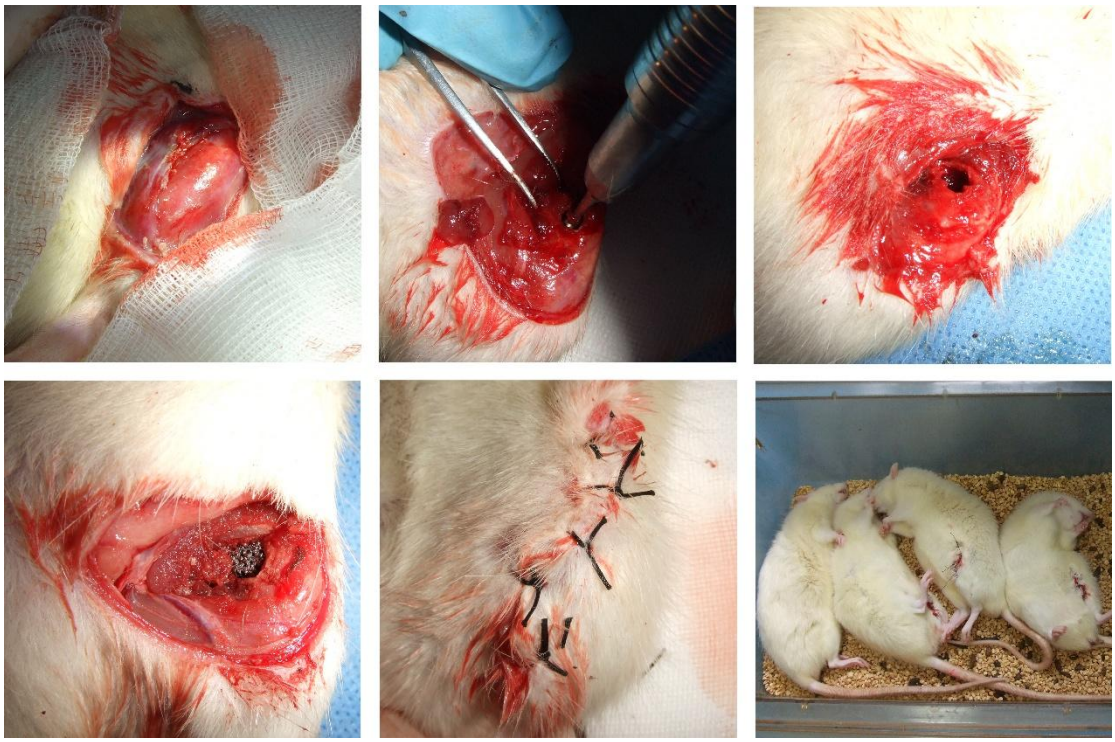


Figure 2. Establishment of a Femoral Defect Model in SD Rats

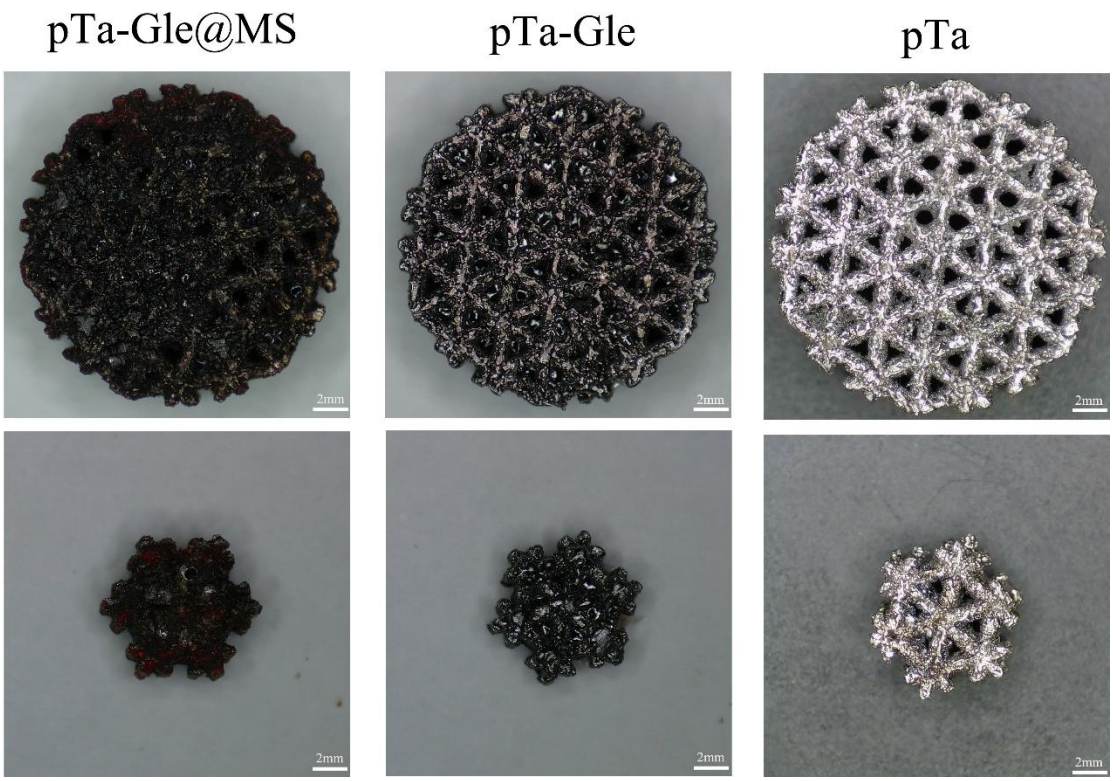


Figure 3. Macroscopic appearance of the 3D-printed porous tantalum composite scaffold loaded with dual-antibiotic microspheres (pTa-Gle@MS), the gelatin-coated porous tantalum scaffold (pTa-Gle), and the unmodified porous tantalum scaffold (pTa).

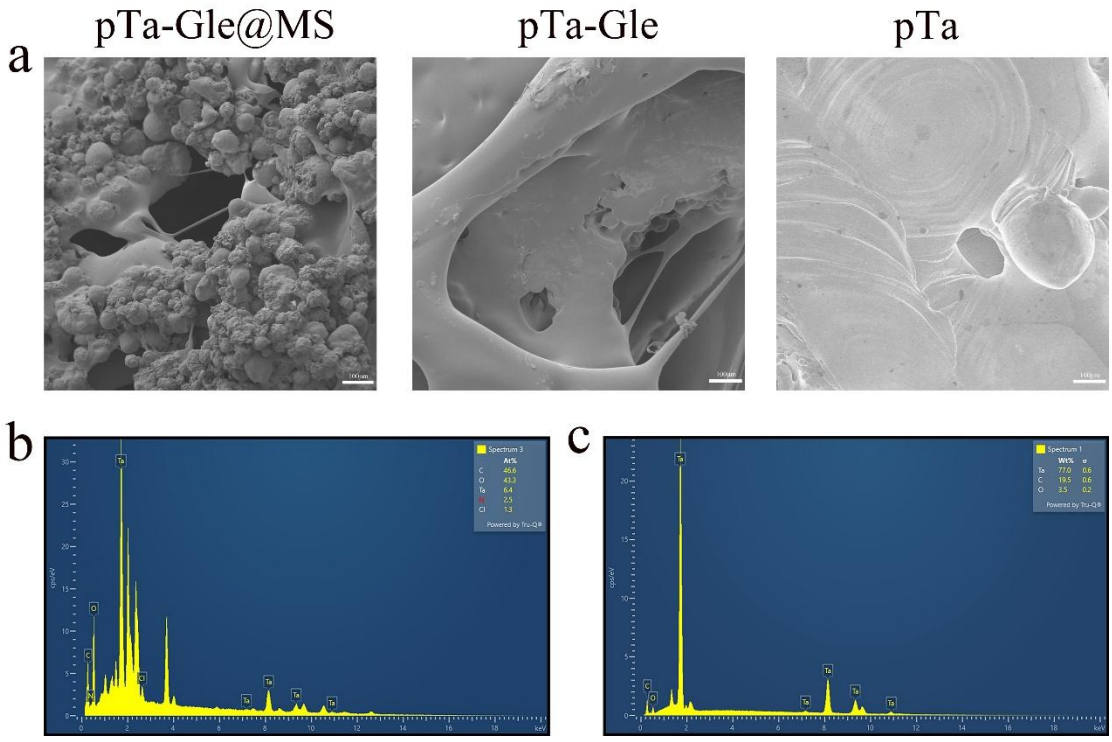


Figure 4. (a) SEM observation of the surface morphology of the scaffold. (b) EDS analysis of the pTa-Gle@MS surface. (c) EDS analysis of the pTa-Gle surface.

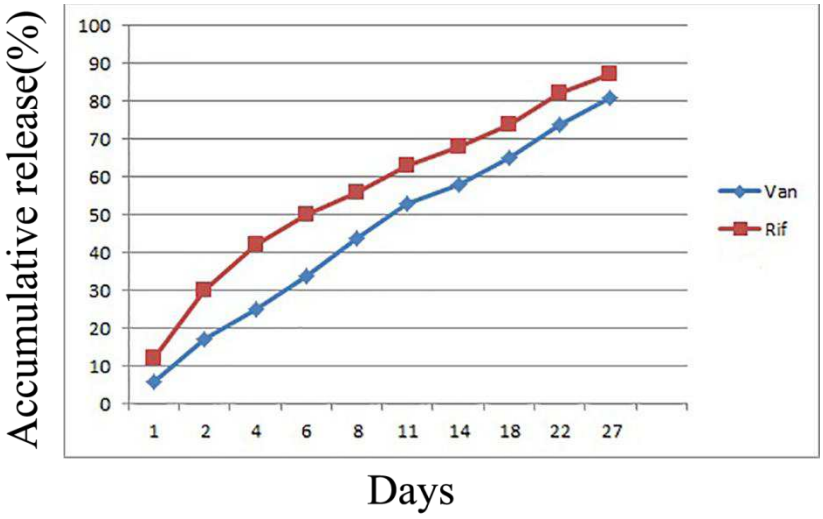


Figure 5. *In vitro* drug-release curve for pTa-Gle@MS.

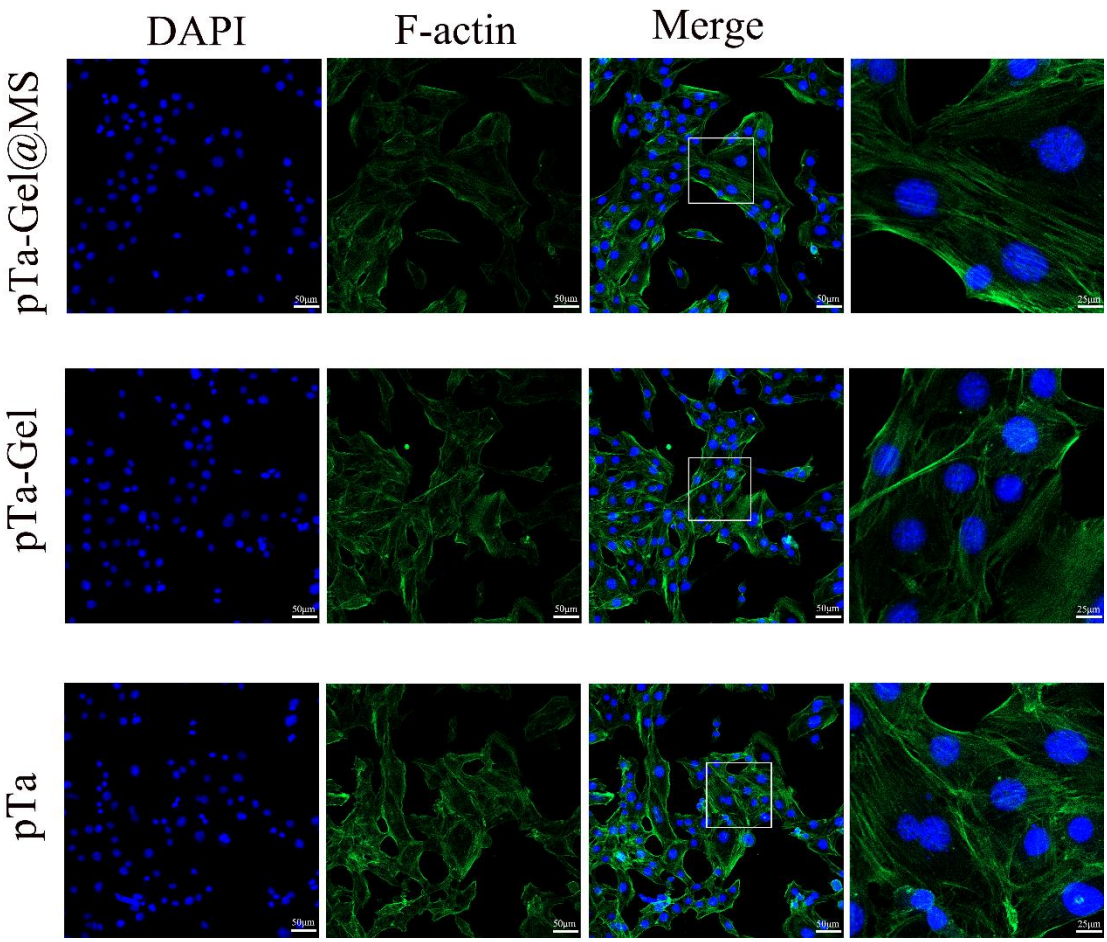


Figure 6. Visualization of cytoskeletal organization in cells seeded on the scaffold surface via CLSM.

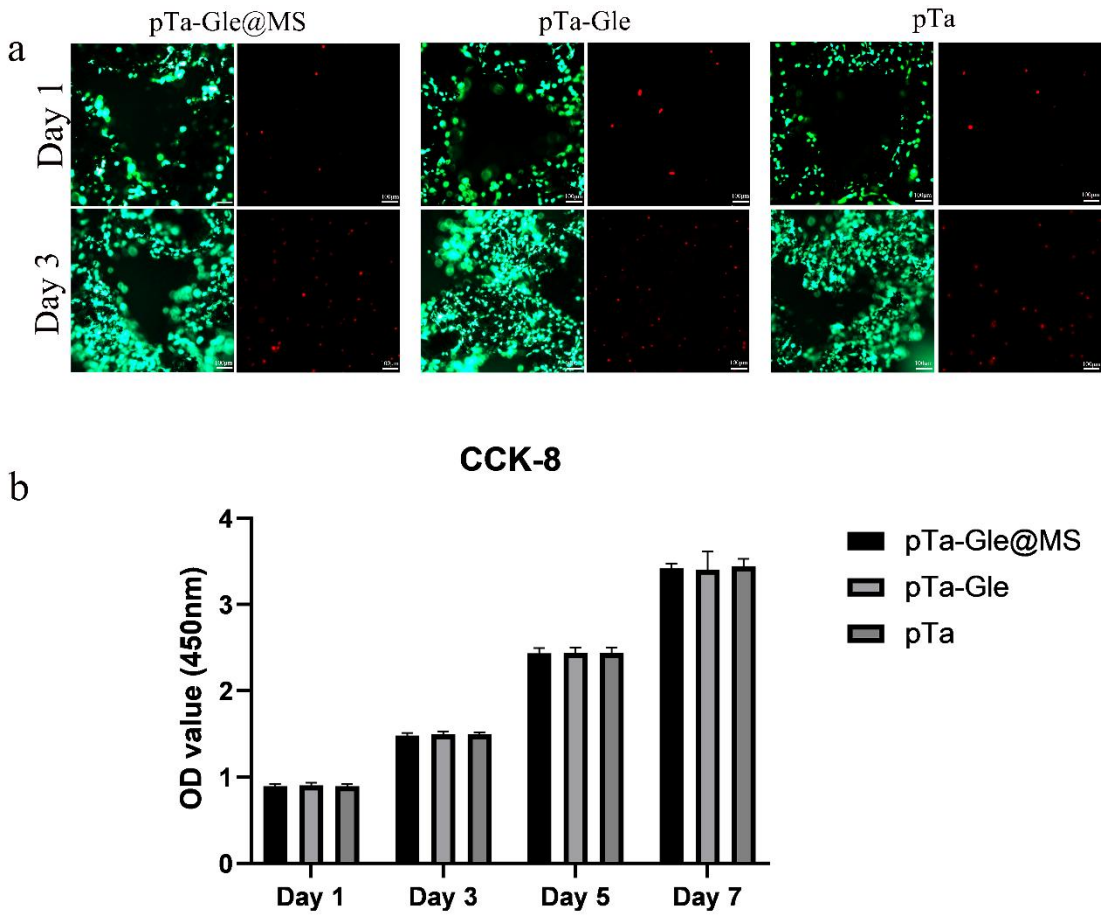


Figure 7. Viability and proliferation of MC3T3-E1 cells exposed to different scaffold formations, as determined by (a) Live/Dead cell staining and (b) CCK-8 assay.

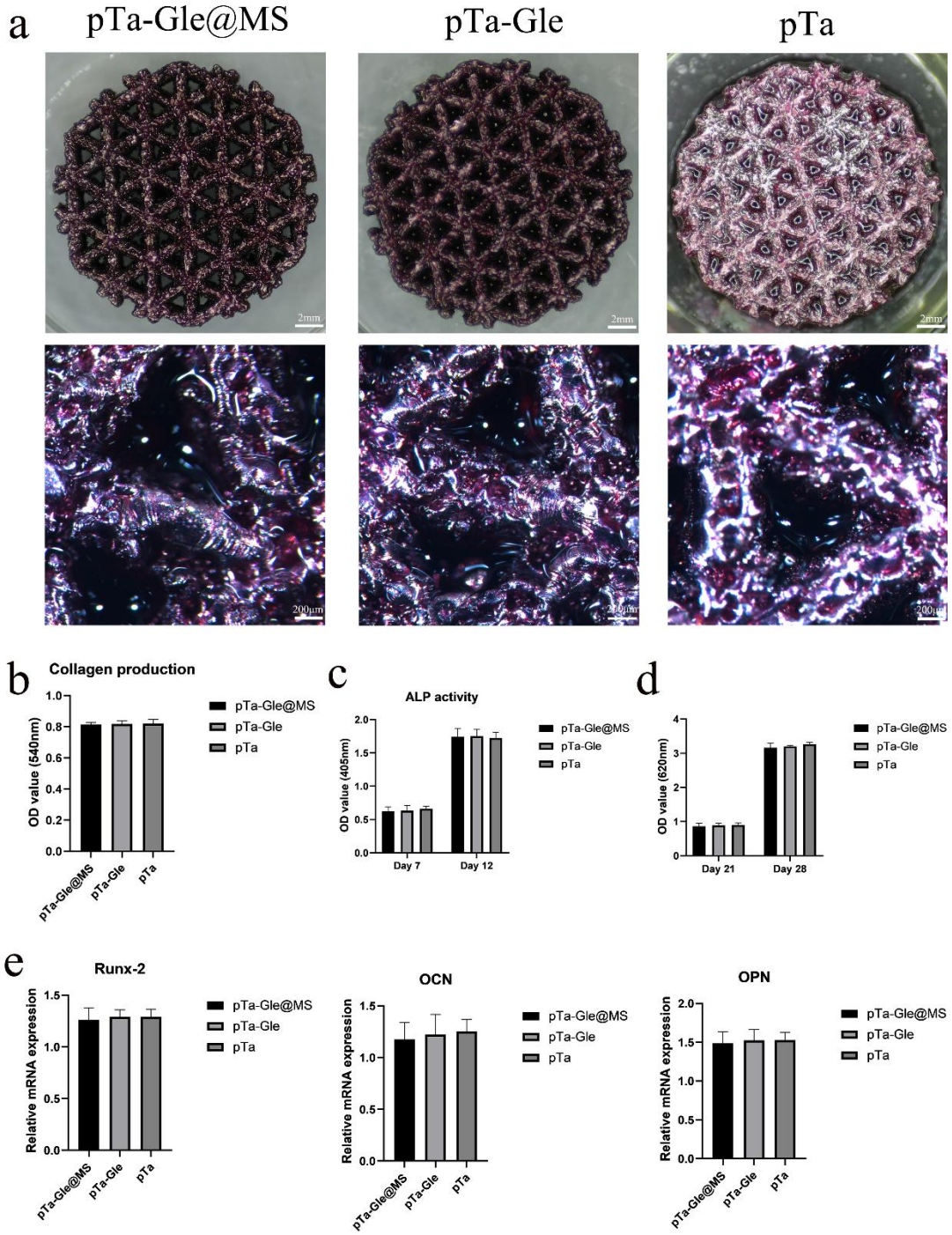


Figure 8. Osteogenic differentiation of MC3T3-E1 cells cultured on different scaffold groups was evaluated by (a) Sirius Red staining for collagen fiber detection with corresponding (b) quantitative analysis, (c) alkaline phosphatase (ALP) staining for quantitative assessment of osteoblastic differentiation, (d) Alizarin Red S staining for quantitative analysis of calcium nodule deposition, and (e) relative expression levels of the osteogenic differentiation genes Runx2, OCN, and OPN.

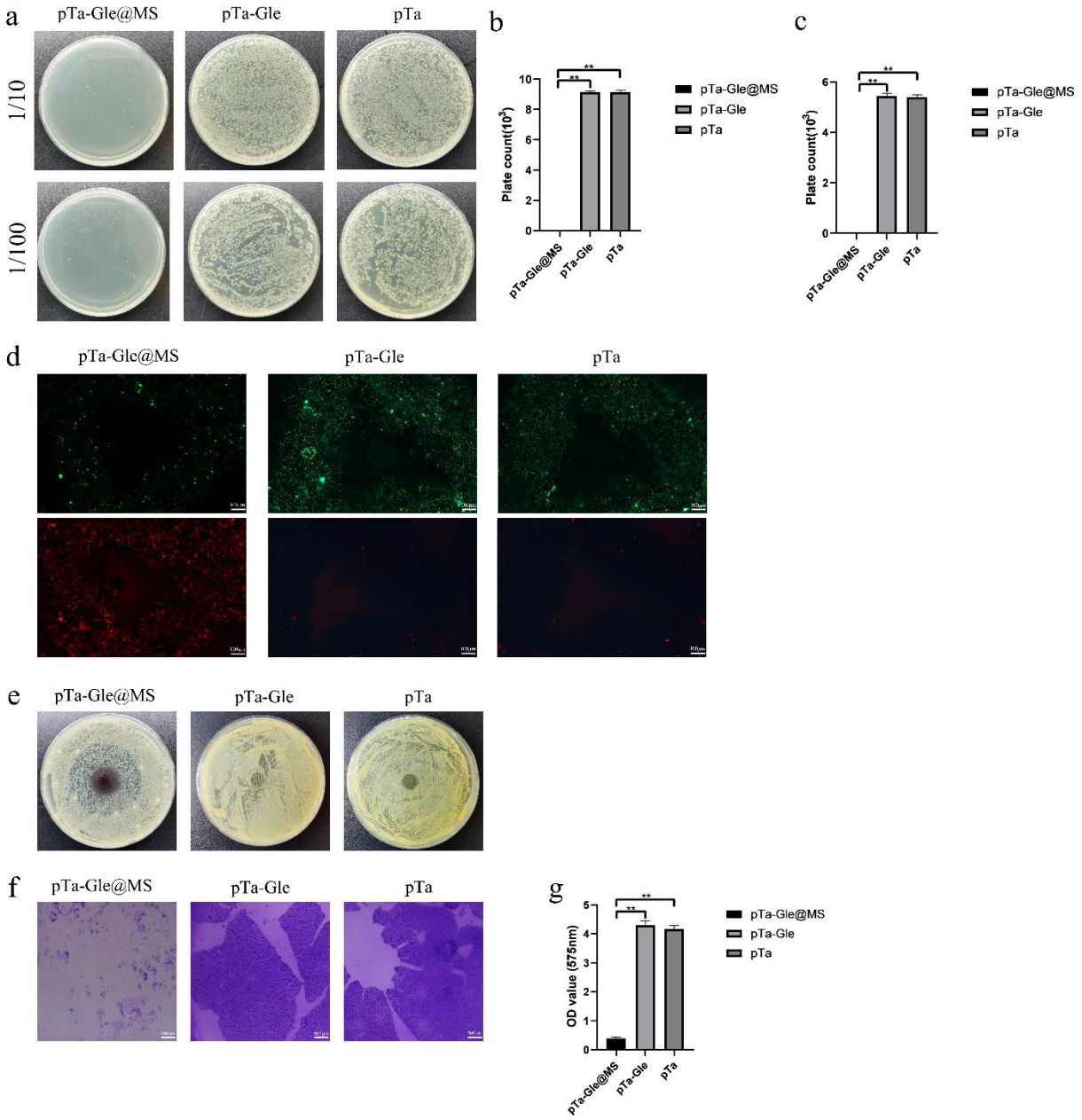


Figure 9. *In vitro* antibacterial efficacy of 3D-printed porous tantalum scaffolds loaded with dual-antibiotic microspheres. (a) After 24 h of exposure to microspheres, the supernatant of *S. aureus* cultures was collected, diluted 10-fold and 100-fold, and then plated. Bacterial concentrations in the culture medium were determined via plate counting for the samples diluted 10-fold (b) and 100-fold (c). The antibacterial effects of the microsphere were further investigated by (d) Live/Dead bacterial staining; (e) zone of inhibition analysis; (f) Crystal Violet staining, and (g) quantitative analysis of bacterial biofilms.

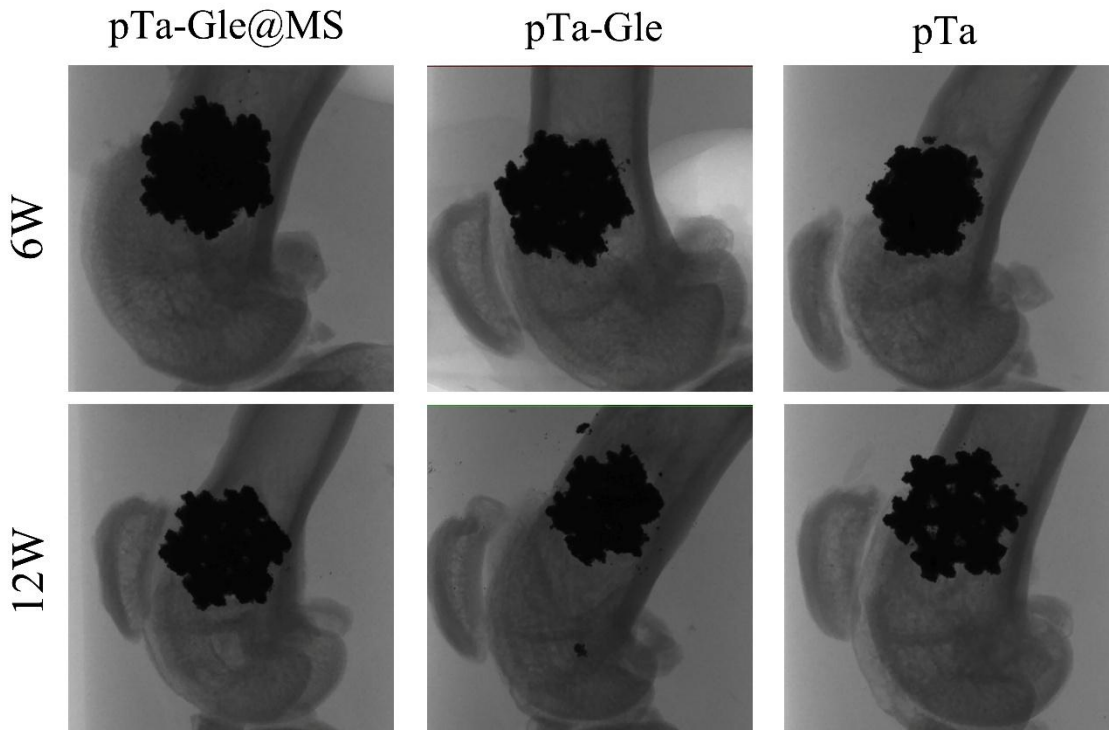


Figure 10. X-ray examination of the femur was performed in SD rats following scaffold implantation in each group.

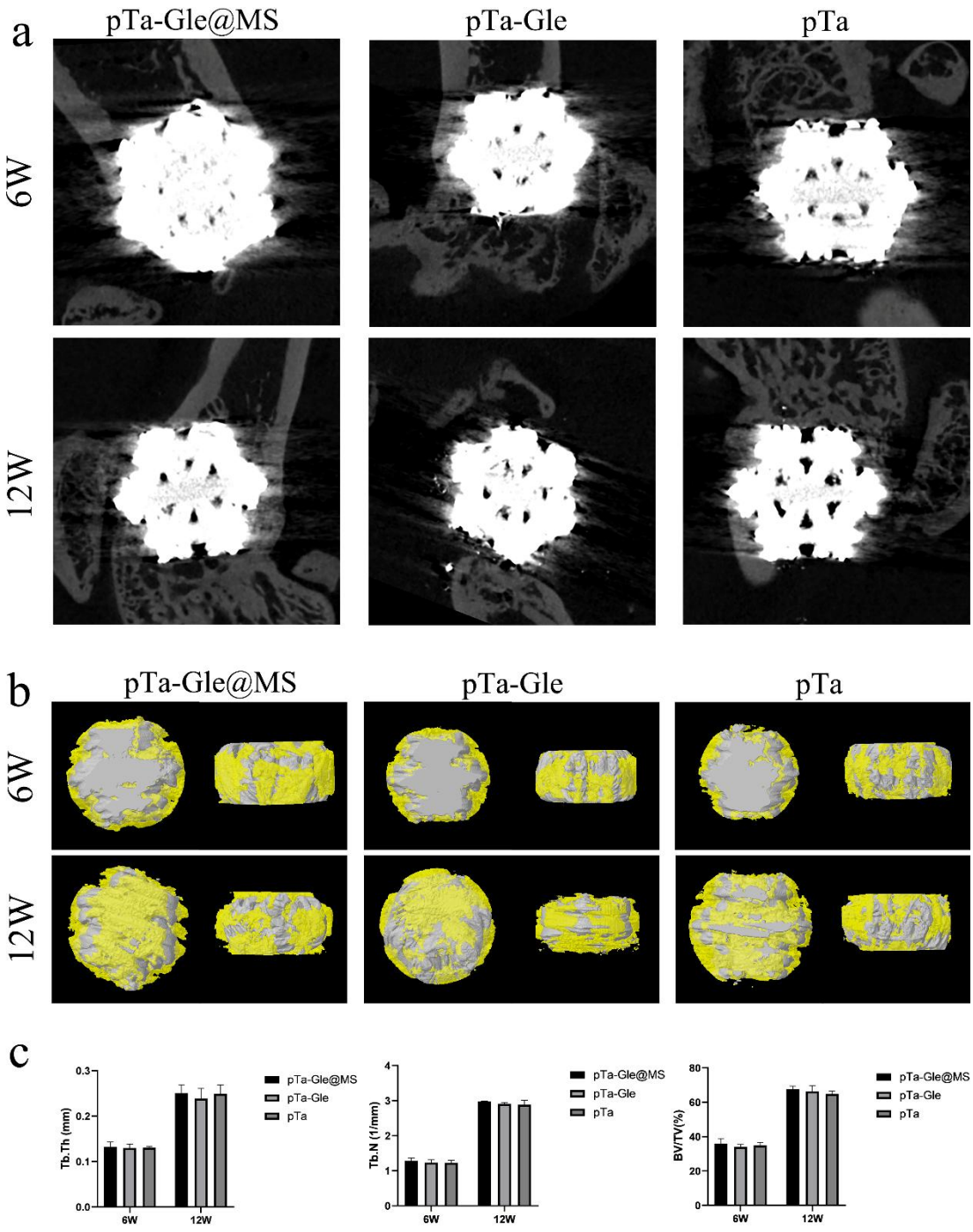


Figure 11. (a) Micro-CT thin-slice high-resolution scanning of the SD rat femur at 6 and 12 weeks post-surgery; (b) Three-dimensional micro-CT reconstructions, with the scaffold shown in gray and bone tissue in yellow; and (c) micro-CT scanning of new bone tissue parameters in each group.

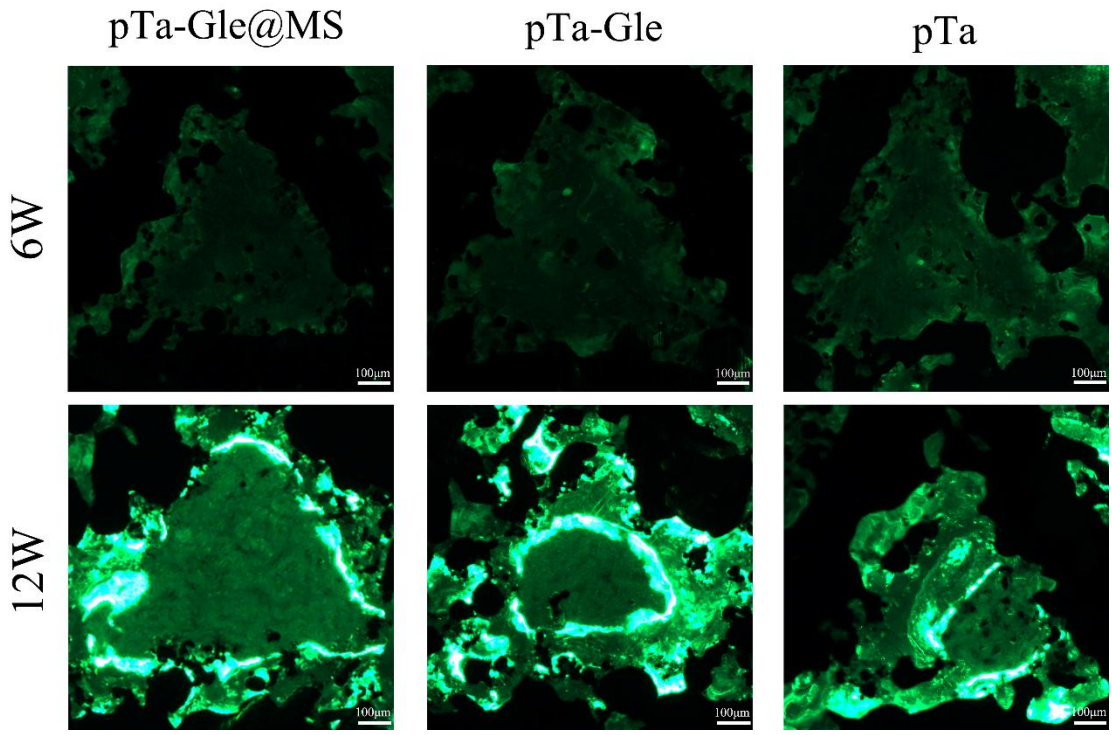


Figure 12. Calcein-labeled newly formed bone tissue within the scaffold pores in each group.

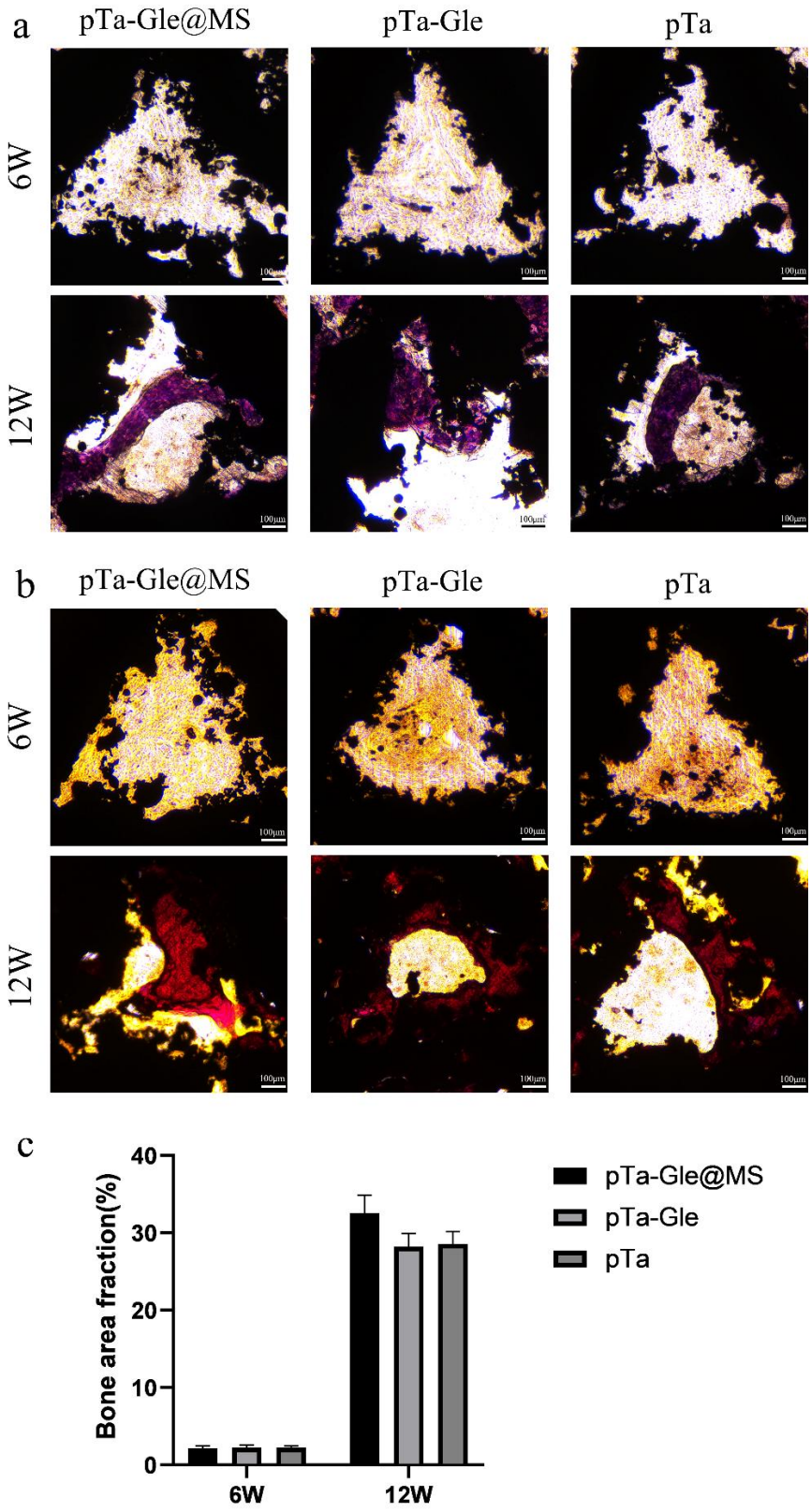


Figure 13. (a) Hematoxylin and eosin (H&E) staining and (b) Van Gieson (VG) staining of bone tissue within the scaffold pores in each group, and (c) percentage of newly formed bone area within the scaffold pores in each group.